Rovibrational wave-packet manipulation using shaped midinfrared femtosecond pulses toward quantum computation: Optimization of pulse shape by a genetic algorithm

Masaaki Tsubouchi and Takamasa Momose*

Department of Chemistry, The University of British Columbia, 2036 Main Mall, Vancouver, British Columbia, Canada V6T 1Z1 and CREST, Japan Science and Technology Agency, Kawaguchi, Saitama, 332-0012, Japan

(Received 29 November 2007; published 20 May 2008)

We have numerically examined optimization of the experimentally achievable shapes of mid-infrared femtosecond laser pulses to construct elementary quantum gates using molecular rovibrational states of a single molecule. Instead of optimizing the electric field by optimal control theory, the method generally used in theoretical studies of coherent control, the transmittance and the phase shift of conventional pulse shapers were optimized in the frequency domain by a genetic algorithm. The target molecular system we examined was the rotation-vibration states of CO in the $X(^1\Sigma^+)$ ground electronic state. Although the existence of the rotational degrees of freedom makes the quantum gate operation complicated, high fidelity of over 0.95 was achieved for one-rovibrational-qubit systems, which indicates that a molecular quantum computer may be feasible for at least one-qubit calculations on a diatomic molecule. On the other hand, two-qubit calculations are more difficult to achieve in a single CO molecule using rotational and vibrational degrees of freedom as different qubits. The importance of the control of the rotational in addition to the vibrational wave packet in order to realize a molecular quantum computer is discussed.

DOI: 10.1103/PhysRevA.77.052326 PACS number(s): 03.67.Lx, 33.20.Xx, 42.55.−f, 03.67.Mn

I. INTRODUCTION

Coherent control of molecules by means of wave packet manipulation has been investigated theoretically in the last two decades, and its experimental realization has been achieved by tailored ultrashort laser pulses [1]. One of the potential applications of coherent control of molecules by shaped ultrashort laser pulses is quantum computation. Molecules have many vibrational (v) and rotational (J) degrees of freedom that are nearly orthogonal to each other. If one can use such internal states in a single molecule as multiple qubits, molecular qubits might have an advantage in terms of scalability. Technically, quantum gate operations by tailored ultrashort laser pulses are more difficult than coherent control of chemical reactions. In the latter, one needs to realize only a specific target state by controlling the wave packet. For such a control, stimulated Raman adiabatic passage (STIRAP) [2–4] is a simple but powerful technique, because it achieves 100% population transfer in a specific transition [5,6]. On the other hand, the former requires unitary transformation among multiple states involving time reversal transitions, which makes the control more difficult [7,8]. For example, the NOT gate operation ($|1\rangle \leftrightarrow |0\rangle$), which is one of the simplest one-qubit gates, requires simultaneous realization of forward ($|1\rangle \leftarrow |0\rangle$) and backward ($|1\rangle \rightarrow |0\rangle$) transitions between two states. Such control cannot be achieved by STIRAP, since the time ordering of the pulse sequence is very important in the STIRAP process, which results in a one-way control only. At the moment, manipulation by shaped ultrashort pulses is the only method to realize desired unitary transformations for quantum gate operations.

The Deutsch-Jozsa algorithm [9], which is one of the elemental algorithms in quantum computation, has been examined both theoretically and experimentally using electronic excited states of Li_2 [10] and I_2 [11] manipulated by arbitrarily shaped laser pulses. Experimentally, manipulation of wave packets in electronic excited states via "rotational-vibronic" transitions from the ground electronic state is less difficult compared with that in the electronic ground state via "rovibrational" transitions because of its large transition moment and the availability of shaped pulses in the visible region. Recently, techniques of arbitrary pulse shaping in the mid- and near-infrared regions have also been established [12–17], which make it possible to apply control in the electronic ground state of molecules [18].

Manipulation of wave packets in the electronic ground state is more appropriate for quantum gate operations because of its long decoherence time (>100 ms). De Vivie-Riedle and co-workers proposed that the normal modes of molecular vibrations manipulated by the shaped mid-ir pulse can be used as qubits [19]. Quantum gate operations by shaped mid-ir pulses with two vibrational normal modes have been examined theoretically for acetylene [20–24] and $MnBr(CO)_5$ [25]. Babikov also investigated quantum gate operations using OH molecules theoretically [26]. In these works, the shapes of mid-ir pulses were optimized by optimal control theory (OCT) to realize quantum gate operations with high fidelity under the assumption that the effect of rotational degrees of freedom is negligibly small. As rotational motion of molecules, however, always couples with vibrational motion in real systems, the effect of the rotation of molecules should not be ignored in calculations of molecular quantum gate operations [27]. Yamashita and coworkers have considered the effect of rotation explicitly, and investigated the optimal control of "rovibrational" wave packets for quantum computation using shaped pulses [28,29]. Their optimized shaped pulses contained frequencies from the mid-ir to the microwave region. Since shaped ultrashort laser pulses have not been experimentally realized in

*momose@chem.ubc.ca

the microwave and far-infrared regions yet, experimental realization of these shaped pulses is not possible at this moment.

In this study, we have numerically investigated the shapes of ultrashort mid-ir pulses which manipulate rovibrational wave packets, and examined the feasibility of applying vibrational-rotational states of a single molecule to one- and two-qubit quantum gate operations. We restricted ourselves to experimentally achievable pulses in order to examine experimental feasibility. In typical pulse shaping methods, a transform-limited laser pulse is manipulated in both amplitude and phase in the frequency domain using liquid crystal spatial light modulator (LC-SLM) [30] or acousto-optic modulator (AOM) [31] devices. Therefore, we optimized the amplitude and phase of mid-ir pulses in the frequency domain. For the optimization, we adopted a genetic algorithm (GA) [32] rather than the commonly used OCT. The OCT is a rapidly convergent iteration method [33–35], in which the laser field is optimized in the time domain in order to achieve a target transition with a large transition probability while minimizing the laser pulse intensity [7,36–39]. The OCT, however, is not appropriate to obtain pulse shapes that are attainable in practical experiments, where pulse shapes are restricted by the bandwidth and amplitude of the input pulse as well as the spectral resolution and dynamic range of pulse shaping devices in the frequency domain. Such restrictions cannot be easily implemented in OCT algorithms, and few works have been reported to implement the spectral constraint [40,41]. On the other hand, since the GA is an indeterministic algorithm and does not require any mathematical and physical information from the previous iteration step in order to obtain solutions in the next iteration step, we can easily impose experimental restrictions on each step in order to optimize laser fields [42].

The present paper is organized as follows. In Sec. II, we summarize the theoretical aspects of the quantum gate operations and the genetic algorithm we employed in the present calculation. Optimized pulse shapes for typical quantum gate operations in one- and two-qubit systems are given in Sec. III together with the wave packet propagation induced by the optimized pulses. In Sec. IV, some conclusions and future perspectives are given.

II. THEORY

A. Molecular qubit system

In the present calculation, rovibrational eigenstates in the ground electronic state $X(^1\Sigma^+)$ of a carbon monoxide (CO) molecule are considered as qubits. We assume that we prepare ultracold molecules that occupy only the $|v=0,J=0\rangle$ state before the manipulations. This assumption is important for the initialization of the qubit system. Since we treat a diatomic molecule in this paper, we use its vibrational degree of freedom (v) as qubit states for a one-qubit calculation. For two-qubit calculation, we consider the vibrational degree of freedom (v) as one qubit and the rotational degree of freedom (J) of the same molecule as another qubit, and examine the feasibility of using different degrees of freedom on a single molecule for quantum gate operations. Throughout this study, we fix the projection quantum number M of the total angular momentum J to be $M=0$, since the rovibrational state is initialized to the state with $J=M=0$.

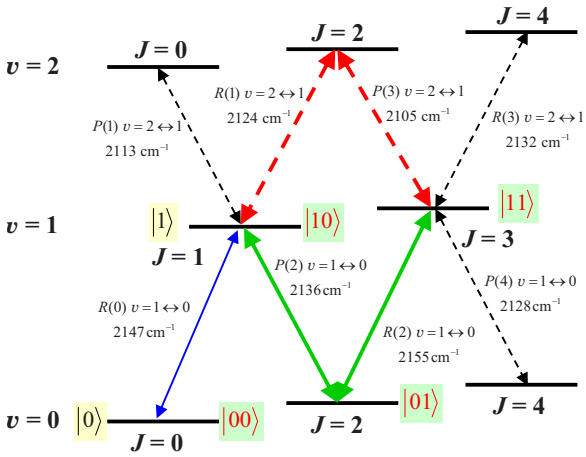

FIG. 1. (Color online) Schematic diagram of rovibrational states in the $X(^1\Sigma)$ ground electronic state of CO. Only the levels accessible from the $|v=0,J=0\rangle$ state by mid-ir photons are shown. The thick solid (green), thick dashed (red), thin solid (blue), and thin dashed (black) lines correspond to the transitions whose frequencies are shown by arrows with the same colors and styles in Figs. 6 and 8. The symbols $R(J)$ and $P(J)$ represent the spectroscopic rotation for the transitions $v+1,J+1\leftrightarrow v,J$ and $v+1,J-1\leftrightarrow v,J$, respectively. The number next to each double arrow shows the transition frequency in units of cm^{-1}.

Figure 1 shows the rotational-vibrational energy levels of a CO molecule. Only the levels accessible from the $|v=0,J=0\rangle$ state by mid-ir photons are shown. In the case of infrared transitions within the $X(^1\Sigma^+)$ state of CO, transitions of $v+1$, $J-1\leftrightarrow v$, J (called the P branch in spectroscopic notation) and $v+1$, $J+1\leftrightarrow v$, J (called the R branch) are only allowed by the one-photon process. Therefore, it is practical to assign the rovibrational states of $|v=0,J=0\rangle$ and $|v=1,J=1\rangle$ as qubits $|q_1\rangle=|0\rangle$ and $|1\rangle$, respectively, for a one-qubit system, and the $|v=0,J=0\rangle$, $|v=0,J=2\rangle$, $|v=1,J=1\rangle$ and $|v=1,J=3\rangle$ states as qubits $|q_1q_2\rangle=|00\rangle$, $|01\rangle$, $|10\rangle$, and $|11\rangle$, respectively, for a two-qubit system, when we manipulate these states by mid-ir radiation only. One may think that the definition of, for example, $|v=0,J=0\rangle$, $|v=0,J=1\rangle$, $|v=1,J=0\rangle$, and $|v=1,J=1\rangle$ as qubits of $|q_1q_2\rangle=|00\rangle$, $|01\rangle$, $|10\rangle$, and $|11\rangle$, respectively, for a two-qubit system, is better and more convenient than our definition in order to avoid unnecessary confusion. Actually such a definition has been employed in previous works [29]. The disadvantage of the latter definition, however, is that the states $|v=0,J=1\rangle$ and $|v=1,J=0\rangle$ are not accessible from the $|v=0,J=0\rangle$ state using mid-ir pulses. Therefore, in order to realize quantum gate operations with the latter definition, one needs shaped pulses in both mid-ir and microwave frequency regions as discussed by Shioya *et al.* [29]. Such shaped pulses are difficult to realize at the present stage.

When we construct a one-qubit system with the $|v=0,J=0\rangle$ and $|v=1,J=1\rangle$ rovibrational states, the former state couples with only the $|v=1,J=1\rangle$ state by a one-photon process in the mid-ir region, but the latter state couples with

four rovibrational states $|v=0,J=0\rangle$, $|v=0,J=2\rangle$, $|v=2,J=0\rangle$, and $|v=2,J=2\rangle$ as shown in Fig. 1. Therefore, one has to suppress the transitions between the $|v=1,J=1\rangle$ state and the $|v=0,J=2\rangle$, $|v=2,J=0\rangle$, and $|v=2,J=2\rangle$ states by shaping the mid-ir pulses in order to achieve high fidelity in quantum gate operations. For a two-qubit system, there are many more transitions that have to be suppressed. Therefore, the difficulty of quantum gate operations using rovibrational states on a single molecule grows drastically as we increase the number of qubits.

B. Quantum gate operations

Since any unitary transformation in the Hilbert space can be decomposed into a product of a controlled-NOT (CNOT) gate of a two-qubit system and a unitary transformation of a one-qubit system, it is only necessary to obtain electric fields that achieve the gate operations of CNOT and representative examples of unitary transformations in order to show the feasibility of quantum gate operations using molecular rovibrational states. By employing the GA described in Sec. II C, we obtained pulse shapes that realize the Hadamard (H), NOT (X), and Pauli-Z (Z) gates that are described by the following matrix forms:

$$H=\frac{1}{\sqrt{2}}\begin{pmatrix}1 & 1\\ 1 & -1\end{pmatrix},\quad X=\begin{pmatrix}0 & 1\\ 1 & 0\end{pmatrix},\quad \text{and}\quad Z=\begin{pmatrix}1 & 0\\ 0 & -1\end{pmatrix}, \tag{1}$$

respectively, for a one-qubit system $|0\rangle$ and $|1\rangle$. We also examined the CNOT gate written in the basis of $|00\rangle$, $|01\rangle$, $|10\rangle$, and $|11\rangle$ as follows:

$$U_{\mathrm{CNOT}}=\begin{pmatrix}1 & 0 & 0 & 0\\ 0 & 1 & 0 & 0\\ 0 & 0 & 0 & 1\\ 0 & 0 & 1 & 0\end{pmatrix}. \tag{2}$$

In Eq. (2), we treated the vibrational and rotational states as the control (q_1) and target (q_2) bits, respectively, based on the definition of qubits described in the previous section. In the optimization of the electric field, we evaluated the following transitions simultaneously in each quantum gate operation. They are

$$|0\rangle \leftrightarrow \frac{1}{\sqrt{2}}(|0\rangle+|1\rangle),\quad |1\rangle \leftrightarrow \frac{1}{\sqrt{2}}(|0\rangle-|1\rangle)$$

for the Hadamard gate, (3a)

$$|0\rangle \leftrightarrow |1\rangle \quad \text{for the NOT gate,} \tag{3b}$$

$$|0\rangle \leftrightarrow |0\rangle,\quad |1\rangle \leftrightarrow -|1\rangle \quad \text{for the Pauli-}Z\text{ gate,} \tag{3c}$$

and

$$|00\rangle \leftrightarrow |00\rangle,\quad |01\rangle \leftrightarrow |01\rangle,\quad |10\rangle \leftrightarrow |11\rangle$$

for the CNOT gate. (3d)

Double-sided arrows show the time-reversible transitions, and both pathways should be achieved simultaneously by a single pulse. For example, for the NOT gate calculation, we calculated wave packet propagation under a shaped pulse from both the $|0\rangle$ and $|1\rangle$ states, and optimized the pulse shape so that $|0\rangle \rightarrow |1\rangle$ and $|1\rangle \rightarrow |0\rangle$ transformations can be achieved simultaneously by the same pulse.

As Tesch and de Vivie-Riedle [23] pointed out, the phase correction should be taken into account in the optimization to achieve all transitions of each quantum gate in phase. For instance, the CNOT gate requires the following transition for the superposition state,

$$|00\rangle+|01\rangle+|10\rangle+|11\rangle \rightarrow (|00\rangle+|01\rangle+|11\rangle+|10\rangle)e^{i\varphi}, \tag{4}$$

where φ is the phase evolution of the total system during the CNOT gate. In order to evaluate the phase correction as well as the population transfer in quantum gate operations, we have calculated the fidelity [8,29] defined as

$$F=\frac{1}{Z^2}\left|\sum_{k=1}^{Z}\langle\Psi_k(t\rightarrow\infty)|\Phi_k\rangle\right|^2, \tag{5}$$

where $|\Psi_k(t\rightarrow\infty)\rangle$ is the wave packet created for a transition k in a specific quantum gate generated after the interaction with a shaped pulse, $|\Phi_k\rangle$ is the wave function of the target state ideal for the transition k, and Z is the number of transitions evaluated in the quantum gate. The fidelity becomes unity if the quantum gate operations are completely realized in both population transfers and phase changes.

C. Optimization method

In order to find the optimal electric field for a specific quantum gate operation, we employed the genetic algorithm implemented for the shaping of femtosecond laser pulse by Zeidler *et al.* [43]. We imposed a condition on the optimization such that the optimized shaped pulse must be generated from a transform-limited pulse that can be obtained by conventional laser systems. The electric field of the input pulse was modeled as

$$E(\omega)=E_0\exp\left[-2\ln 2\left(\frac{\omega-\omega_c}{\Delta\omega}\right)^2\right]\exp[i\phi(\omega)], \tag{6}$$

where E_0 is the peak intensity of the field, $\omega=2\pi\nu$ is the angular frequency, and $\omega_c=2\pi\nu_c$ is the center frequency which resonates with the $v=1\leftrightarrow v=0$ vibrational transition of CO, $\nu_c=64.4$ THz (2147 cm^{-1}). The phase of the input pulse in Eq. (6) was set to be $\phi(\omega)=0$, that is, the transform-limited pulse. The full width at half maximum (FWHM) of the angular frequency $\Delta\omega=2\pi\Delta\nu$ of the input pulse depends on the laser system. We assumed the width of $\Delta\nu=3$ THz (100 cm^{-1}) which corresponds to a time width of $\Delta t=147$ fs for the FWHM. As for the integrated input laser intensity (pulse energy) $I=c\varepsilon_0\int d\omega|E(\omega)|^2$, we assumed intensities of 5–30 μJ/pulse (the peak intensity of 1–10 TW/cm^2 for a transform-limited pulse with $\Delta t=147$ fs focused down to 50 μm in diameter), which are the maximum intensities available by commercial laser systems in the mid-ir region at the present.

We also imposed a condition that shaped pulses are the ones obtainable by conventional pulse shapers. Any conventional pulse shaper has a spectral resolution $\delta\omega$. The transmittance $[0 \le f(\omega_j) \le 1]$ and phase shift $[0 \le \phi'(\omega_j) < 2\pi]$ at frequency ω_j for $\omega_j = \omega_c \pm j\ \delta\omega$ $(j=0, \pm 1, \ldots, \pm N)$ applied by a shaper are the parameters to be optimized by the GA, which yields the output spectrum

$$E'(\omega_j) = E_0 \sqrt{f(\omega_j)} \exp\left[-2\ln 2 \left(\frac{\omega_j - \omega_0}{\Delta\omega} \right)^2 \right] \exp[i\phi'(\omega_j)]. \tag{7}$$

We therefore have $4N+2$ parameters to be optimized in a GA loop. In practice, the output shaped spectra obtained using a LC-SLM shaper are discrete. On the other hand, the spectra shaped by an AOM are convoluted by the frequency resolution of the AOM. In the present calculation, we have taken into account the spectral resolution of the shaper for the case of an AOM shaper, and interpolated the discrete spectra by employing the cubic spline interpolation method [44].

Here, we briefly review the genetic algorithm we used in the present calculation. As the parameter sets for iterations, we introduced P vectors $\{\mathbf{x}_1, \mathbf{x}_2, \ldots, \mathbf{x}_P\}$, in which each vector set consists of $4N+2$ parameters as $\mathbf{x}_p = (x_1^p, x_2^p, \ldots, x_{4N+2}^p)$ for the pth vector. As described above, $2N+1$ parameters among the $4N+2$ describe the transmittance and the others describe the phase shift at each frequency. Each value x_n^p takes a non-negative integer value between 0 and $K-1$, where K is the dynamic range of the pulse shaper. These integers x_n^p were converted into the transmittance and phase shift at each frequency such that the transmittance takes the value of $f(\omega_{(n-1)/2-N}) = x_n^p/(K-1)$ for odd numbers of n and the phase shift $\phi'(\omega_{n/2-N-1}) = 2\pi x_n^p/K$ for even numbers of n. Note that the values of $f(\omega_j)$ fall between 0 and 1 under such conditions, which assures that the amplitude of the shaped pulse does not exceed the input amplitude at each frequency. The phase shifts are restricted to values between 0 and 2π. Initial sets of the P vectors for the first iteration loop were generated randomly.

In each iteration, the fidelity of quantum gate operations was calculated by Eq. (5) numerically for all P vector sets. Then, the L vectors with the highest fidelity were chosen among the total P vectors as parent vectors. The P child vectors for the next generation were generated by *mutation* and *recombination* processes using the L parent vectors. We did not employ the cloning process, which carries the exact parent vectors to child vectors. Thus, after generating the P child vectors, all the parent vectors were disregarded.

From each parent vector $\mathbf{x}_p$, we generated M child vectors by mutation as follows. Each vector element was changed by the mutation operator with a probability of P_{mut} to construct a child vector $\mathbf{y}_q$ as follows:

$$y_n^q = \begin{cases} x_n^p + \sigma_l m_n, & r_n \le P_{\text{mut}}, \\ x_n^p, & r_n > P_{\text{mut}}. \end{cases} \tag{8}$$

Here, $\mathbf{r} = (r_1, r_2, \ldots, r_{4N+2})$ is a random number sequence with $0 \le r_n \le 1$, which was generated each time. The product $\sigma_l m_n$ describes the amount of shift from the value x_n^p to y_n^q. The factor m_n is a normal random number with a Gaussian probability distribution $P(m_n)$,

$$P(m_n) = \frac{1}{\sqrt{2\pi}} \exp\left(-\frac{m_n^2}{2} \right), \tag{9}$$

and is generated whenever a mutation occurs $(r_n \le P_{\text{mut}})$. The parameter σ_l is the step length for the lth generation, which determines the amount of change by a mutation. The parameter σ_l controls the convergence speed and the convergence properties. As suggested by Zeidler *et al.* [43], in order to achieve fast convergence, the step length at the lth generation loop was changed by the ratio of the number of successful vectors, N_{suc}, created by the mutation in the previous $(l-1)$th generation to the number of vectors created by mutation, N_{tot} $(=ML)$. Successful vectors are those whose fidelity is better than that of their parent vector. Numerically, the step length for the lth generation was calculated by

$$\sigma_l = \begin{cases} \sigma_{l-1} q & (\eta \le \eta_c), \\ \sigma_{l-1}/q & (\eta > \eta_c), \end{cases} \tag{10}$$

where $\eta = N_{\text{suc}}/N_{\text{tot}}$, $\eta_c (0 \le \eta_c \le 1)$ is a threshold value that determines whether the step length is increased or decreased, and $0 < q < 1$ is a contraction factor. The threshold value η_c, contraction factor q, and step length at the first generation, σ_1, determine the convergence behavior in the calculation, and should be carefully determined for each case.

The other $P-ML$ child vectors were generated by a recombination procedure. Two parent vectors $\mathbf{x}_{q'}$ and $\mathbf{x}_{q''}$ $(q' \ne q'')$ were chosen from the L parent vectors at random. As the recombination scheme, we adopted the multiple crossover method which provides a child vector $\mathbf{y}_q$ as follows:

$$y_n^q = \begin{cases} x_n^{q'}, & r_n \le 0.5, \\ x_n^{q''}, & r_n > 0.5, \end{cases} \tag{11}$$

where $\mathbf{r} = (r_1, r_2, \ldots, r_{4N+2})$ is a random number sequence of $0 \le r_n \le 1$ generated for each vector.

In the actual simulation, we employed the following parameters. The input pulse to the shaper was assumed to be the Gaussian pulse shape described by Eq. (6) with $\Delta\nu = 100\ \text{cm}^{-1}$. The spectra of the transmittance and phase shift of the shaper were discretized with a step size of $d\nu = d\omega/2\pi = 300$ GHz $(10\ \text{cm}^{-1})$ in the frequency range of $\pm 250\ \text{cm}^{-1}$ centered at $\nu_c = 64.4$ THz $(2147\ \text{cm}^{-1})$. Therefore, each vector consists of 102 variables, or $N=25$. The dynamic range of the shaper was assumed to be $K=64$. In each generation, we created $P=48$ vectors, calculated the fidelity of each vector as discussed in Sec. II D, and chose $L=8$ vectors with the highest fidelity as parent vectors for the next generation. We generated $M=4$ children from each parent vector by mutation, with the probability $P_{\text{mut}}=0.2$, the threshold value $\eta_c=0.6$, the contraction factor $q=0.95$, and the step length at the first generation, $\sigma_1=20.0$. The number of total child vectors generated by the mutation was 32. Another 16 child vectors were generated by recombination with multiple crossovers. With these parameters, the optimized parameters were converged within 100 generations in most

cases. After 100 generations, we selected the vector with the best fidelity as the optimal parameter set, and calculated the optimal electric field by Eq. (7).

D. Evaluation of optimal electric fields

To evaluate the vectors in each generation, we have calculated the fidelity in Eq. (5) using a wave packet propagated under the electric field in Eq. (7). The calculation method for wave packet propagation employed in the present study was described in our previous paper [27]. Briefly, the time dependence of the molecular wave function $\Psi(t)$ is given by the Schrödinger equation as

$$i\hbar\frac{d\Psi(t)}{dt} = H(t)\Psi(t) = [H_0 + H_1(t) + H_2(t)]\Psi(t). \quad (12)$$

Here, H_0 is the zeroth-order molecular rovibrational Hamiltonian, and $H_1(t)$ and $H_2(t)$ represent the interaction between molecule and laser field via the dipole moment and polarizability, respectively. Since we consider the case where the femtosecond pulse contains a resonant frequency of the vibrational transition, the term of the first-order dipole interaction H_1 is dominant compared with the polarizability term H_2. If the laser pulse does not contain a resonant frequency, the contribution of the dipole interaction term is rapidly diminished due to time averaging. In such a case, the second-order interaction via polarizability becomes more important. The Hamiltonians H_0, $H_1(t)$, and $H_2(t)$ were constructed by the use of experimentally reported spectroscopic constants to calculate the eigenenergies of rovibrational states [45], transition dipole matrix elements [46], and polarizabilities of CO [47]. Details of these terms are derived in our previous paper [27].

The differential equation (12) was integrated using the initial state of each transition in the quantum gate operation described in Eqs. (3a)–(3d) to obtain the propagation of the rovibrational wave function under the electric field in Eq. (7). The calculated wave functions at sufficiently large time t were used to evaluate the fidelity in Eq. (5) with the target states of the gate operation. The propagation time step for solving the differential equation in Eq. (12) was taken as $dt=0.1$ fs, which is much smaller than the oscillation period of the electric field of laser pulses, that is, 16.7 fs for the pulse with the wavelength at 5 μm.

III. RESULTS AND DISCUSSION

In this section, we first present the optimized electric fields for one-qubit gate operations obtained by considering only vibrational degrees of freedom. Then, the optimized electric fields obtained by considering full rovibrational states for both one- and two-qubit operations are given. The purpose of presenting the results for both cases is to discuss the importance of rotational states in evaluating optimized pulse shapes for practical purposes.

A. Optimized electric fields for pure vibrational quantum gates

In this section, we first discuss the optimized electric fields for quantum gate operations using pure vibrational eigenstates as qubits. We ignored the rotational degrees of freedom, and considered the vibrational states of $v=0$ and 1 as the qubits of $|0\rangle$ and $|1\rangle$, respectively. Since rotational excitations are always associated with any vibrational excitation, it is not realistic to ignore the rotational degrees of freedom. Nevertheless, we intentionally present results for pure vibrational gates in order to understand the general behavior of wave packet dynamics.

In order to solve the Schrödinger equation in Eq. (12), we expanded the time-dependent wave function $|\Psi(t)\rangle$ in terms of the vibrational states $|v\rangle$ as

$$|\Psi(t)\rangle = \sum_v C_v(t)|v\rangle, \quad (13)$$

where $C_v(t)$ is the complex amplitude of the state $|v\rangle$, which is the eigenstate of the Hamiltonian H_0 in Eq. (12). We have included from $v=0$ up to 6 states in Eq. (13) as the basis sets. The dipole interaction is described as

$$H_1(t) = -\vec{\mu}\cdot\vec{\varepsilon}(t) = -\mu\varepsilon(t), \quad (14)$$

where μ is the pure vibrational dipole operator and $\varepsilon(t)$ is the electric field of the laser pulse in the time domain, which was calculated by Fourier transformation of the electric field in Eq. (7) as $\varepsilon(t)=\int d\omega\, E'(\omega)\exp(i\omega t)$. The interaction via the polarizability is given by

$$H_2(t) = -\frac{1}{2}\vec{\varepsilon}(t)\cdot\vec{\alpha}\cdot\vec{\varepsilon}(t) = -\frac{1}{2}\varepsilon(t)^2\alpha, \quad (15)$$

where α is the isotropic polarizability operator for pure vibrational states.

1. Hadamard gate

First, we examined the Hadamard gate, which is the fundamental one-qubit gate for algorithms in quantum computing. The optimized laser field was calculated so as to achieve the following four transitions: path (a), $|0\rangle \rightarrow (|0\rangle+|1\rangle)/\sqrt{2}$, path (b), $(|0\rangle+|1\rangle)/\sqrt{2} \rightarrow |0\rangle$, path (c) $|1\rangle \rightarrow (|0\rangle-|1\rangle)/\sqrt{2}$, and path (d) $(|0\rangle-|1\rangle)/\sqrt{2} \rightarrow |1\rangle$, simultaneously.

Figure 2 presents the optimized electric field to achieve the Hadamard gate operation, and Fig. 3 shows the population and phase evolution of each vibrational state through the interaction with the optimized electric field displayed in Fig. 2. Figures 2(a) and 2(b) show the spectrum and the temporal pulse intensity of the shaped pulse, respectively. A laser energy of 7.5 μJ, which has been obtained in previous experimental studies [48–50], was assumed for the input pulse to the shaper in this calculation. The temporal pulse width after the pulse shaper was spread to 4 ps from the initial width of 150 fs. Due to the pulse spreading, the peak intensity of the input pulse, 2.44 TW/cm^2, was reduced to 0.156 TW/cm^2, corresponding to the electric field $\varepsilon=10.8$ MV/cm. The long duration time ($\sim$4 ps) of the pulse was required to realize the Hadamard gate operation, partly because the de-excitation of higher ($v\geq 2$) vibrational states transiently produced by excitation from the $v=1$ state takes some time, as seen in Fig. 3. Here, we treat the transition in the nonperturbative region which is characterized by the Rabi frequency

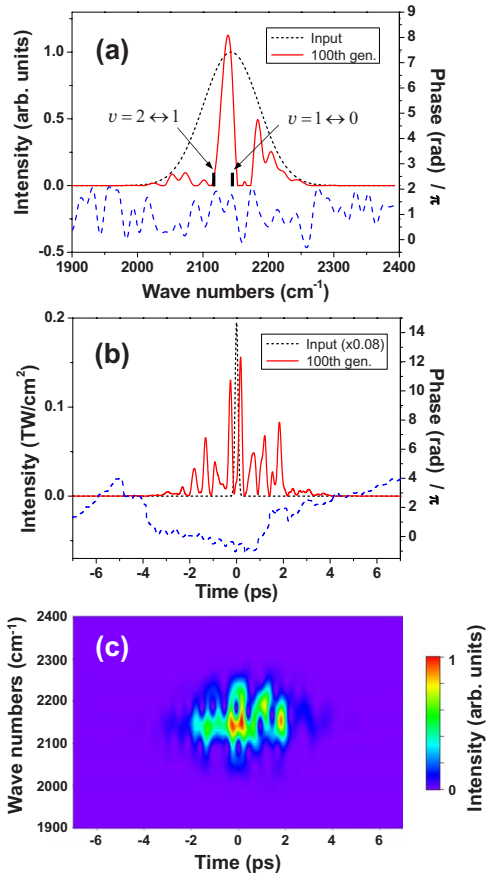

FIG. 2. (Color online) Optimized laser pulse for the Hadamard gate using the pure vibrational eigenstates $|0\rangle$ and $|1\rangle$ in the $X(^1\Sigma^+)$ state of CO as qubits. The pulse shape is shown in (a) the frequency and (b) the time domain, and (c) as the Gabor transform calculated by Eq. (16). Dotted (black) and solid (red) lines show the shape of the input pulse and the optimized pulse after 100 generations of the GA, respectively. Dashed (blue) line shows the optimized phase of the shaped pulse. The bold black lines indicate the transition frequencies for the $v=1\leftrightarrow0$ transition (2143 cm^{-1}) and for the $v=2\leftrightarrow1$ transition (2117 cm^{-1}).

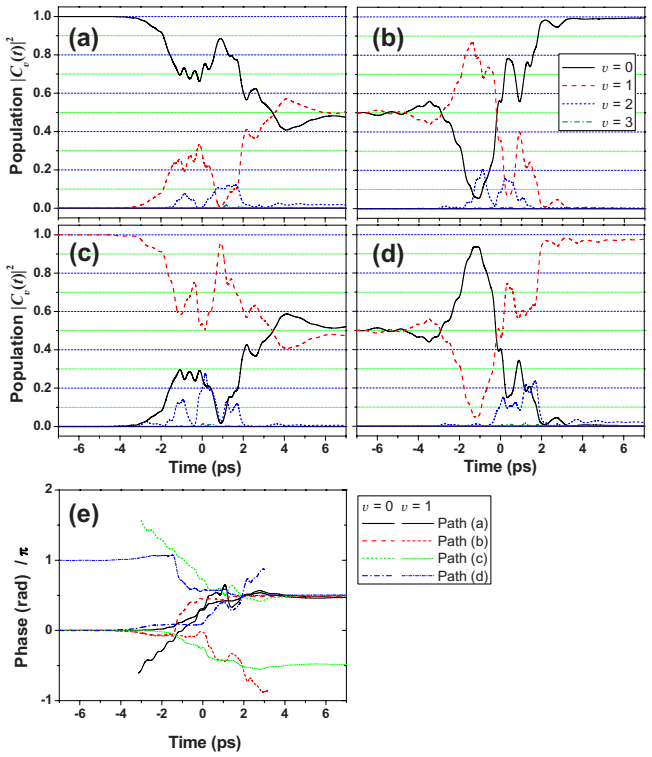

FIG. 3. (Color online) Population transfers and phase changes by the optimized laser pulse shown in Fig. 2 for the Hadamard gate using the pure vibrational eigenstates of CO. Rotational degrees of freedom were ignored. The input pulse energy was 7.5 μJ in the calculation. (a)–(d) display the population changes of paths (a)–(d) in the Hadamard gate, respectively. (e) shows the phase evolution of the vibrational eigenstates composing the wave packet in each path. Note that the phases are shown only when the population of each $v=0$ and $v=1$ state is greater than 5%.

$\omega_R=\mu\varepsilon/\hbar$. In order to deexcite the population from the higher vibrational state, a 2π pulse with the time duration of $\Delta t=2\pi/\omega_R$ is required. This time duration is estimated to be longer than 2 ps, and therefore a long-duration pulse is required for the Hadamard gate. Note that the optimized spectrum shown in Fig. 2(a) exceeds the input pulse intensity at 2138 cm^{-1}; this was artificially caused by the cubic spline interpolation employed in the calculation to obtain a smooth curve between segments in the spectrum. The cubic interpolation is not a linear interpolation method, but uses the second derivatives at the discrete sample points. Therefore, when the second derivative is accidentally large, the interpolated values at certain frequencies can exceed the intensity of the input pulse. We believe that this numerical error does not significantly affect the entire behavior of the wave packet propagation.

Figure 2(c) shows the time-resolved power spectrum of the optimized laser field expressed by the Gabor transformation, which is defined as

$$F(\omega,\tau)=\left|\int dt\, H(t-\tau,\Delta)\varepsilon(t)\exp(i\omega t)\right|^2, \qquad (16)$$

where $H(t,\Delta)$ is the Blackman window [51],

$$H(t,\Delta)=\begin{cases}0.08\cos\left(\dfrac{4\pi t}{\Delta}\right)+0.5\cos\left(\dfrac{2\pi t}{\Delta}\right)+0.42 & \text{if } |t|\le\dfrac{\Delta}{2},\\ 0 & \text{if } |t|>\dfrac{\Delta}{2},\end{cases} \qquad (17)$$

and Δ determines the time resolution of the two-dimensional function $F(w,t)$. Here we have fixed $\Delta=1$ ps. An intricate time-frequency structure of the optimized pulse is displayed in Fig. 2(c).

Figures 3(a)–3(d) show the population changes of each vibrational state for paths (a)–(d), respectively. By applying the optimized laser field, the four transitions in paths (a)–(d) are almost achieved simultaneously, while undesired vibrational climbing is mostly suppressed. During the interaction with the pulse, the population in the $v=2$ state increases up to 20%; this is almost completely suppressed after the interaction.

Figure 3(e) shows the temporal phase profiles of the $v=0$ and 1 vibrational states for paths (a)–(d). Note that the phase is displayed only when the population of the state is greater than 5%, since the phase cannot be well defined in less populated states. As shown in Fig. 3(e), the relative phase can also be well controlled by the optimized laser field, while the total phase change by $\varphi \sim \pi/2$. That is, the transition with phase correlation

$$|0\rangle + (|0\rangle + |1\rangle)/\sqrt{2} + |1\rangle + (|0\rangle + e^{i\pi}|1\rangle)/\sqrt{2} \rightarrow [(|0\rangle + |1\rangle)/\sqrt{2} + |0\rangle + (|0\rangle + e^{i\pi}|1\rangle/\sqrt{2}) + |1\rangle]e^{i\varphi} \quad (18)$$

is realized. Eventually, the result indicates that the Hadamard gate was realized with a fidelity of $F=0.9834$, which corresponds to a quantum gate efficiency of 98.34%.

Our optimized electric field achieved a fairly high fidelity of $F=0.9834$, but there is still a small error in the gate operation. The efficiency of population transition without the phase factor can be evaluated by the following average transition probability [29]:

$$\bar{P} = \frac{1}{Z}\sum_{k=1}^{Z} |\langle \Psi_k(t \rightarrow \infty)|\Phi_k\rangle|^2. \quad (19)$$

The optimized result shown in Fig. 3 gives the value of $\bar{P}=0.9846$, which is almost the same as the fidelity F. Therefore, the residual error is mainly due to insufficient population transfers, but not phase corrections.

2. NOT and Pauli-Z gates

The NOT gate that includes the two transitions path (a) $|0\rangle \rightarrow |1\rangle$ and path (b) $|1\rangle \rightarrow |0\rangle$ was also optimized with the input energy of 10 μJ, and obtained the fidelity of $F=0.9938$. The optimized results are not shown here in the figures. The duration time of the optimized laser pulse was $\sim$6 ps, which is longer than that for the Hadamard gate shown in Fig. 2, and the population was completely inverted after a number of population exchanges, mainly among $v=0$, 1, 2, and 3 states. The NOT gate operation requires a long interaction time, because 100% population transfer needs to be achieved. In the case of the Hadamard gate, only 50% population transfer is required, which makes the duration time shorter (4 ps) than that of the NOT gate operation.

Figure 4 presents the optimized results for the Pauli-Z gate that includes the following three transitions: path (a), $|0\rangle \rightarrow |0\rangle$, path (b), $|1\rangle \rightarrow -|1\rangle$, and path (c), $-|1\rangle \rightarrow |1\rangle$. We illustrated the population transfers and phase changes for only paths (a) and (b) in Figs. 4(a) and 4(b), respectively. The laser energy of 10 μJ was assumed to be input to the shaper in this calculation. The optimized laser field shown in Fig. 4(c) as a Gabor transform realized the Pauli-Z gate with a fidelity $F=0.9943$. In path (a), the population stayed in the $v=0$ initial states mostly during the interaction with the shaped pulse. On the other hand, the population in the $v=1$ state was almost transferred to the $v=2$ or 3 state at -0.5 ps in paths (b) and (c) (not shown), and then transferred back to the $v=1$ state at about 2 ps. As shown in Fig. 4(b), and compared with the phase evolution in path (a) in Fig. 4(a), the phase jumped by π at -0.5 ps when the population was transferred to the $v=2$ or 3 state. This indicates that population transfer to auxiliary levels is necessary at the transient state in order to achieve a π phase rotation. In the present case, the higher vibrational states ($v=2$ or 3) are used as the auxiliary levels. As shown in Fig. 4(c), the laser pulse contains only small intensities at the frequency resonant with the

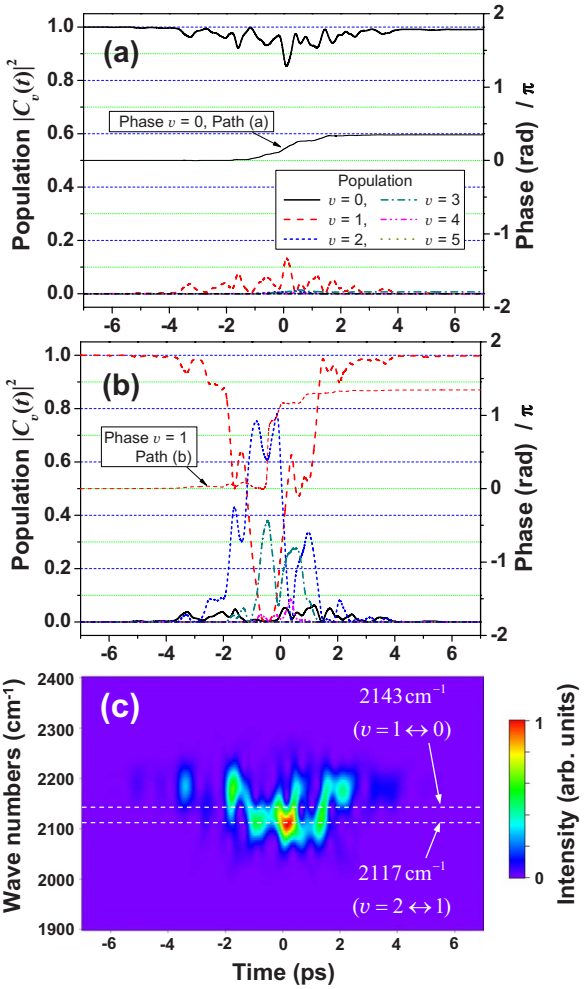

FIG. 4. (Color online) Optimized result for the Pauli-Z gate using the pure vibrational eigenstates. Rotational degrees of freedom were ignored. The input pulse energy was assumed to be 10 μJ in the calculation. Thick lines in (a) and (b) display the population transitions of paths (a) and (b) in the Pauli-Z gate, respectively. The phase profiles are also shown in the same figure as the thin lines. (c) shows the optimized laser pulse for the Pauli-Z gate shown in the Gabor transform calculated by Eq. (16).

TABLE I. The efficiencies of quantum gate operations with pure vibrational eigenstates in the $X(^1\Sigma^+)$ state of CO.

Gate	F	$\bar{P}$	Input energy (μJ)	Peak intensity (TW/cm^2)
Hadamard	0.9834	0.9846	7.5	0.156
NOT	0.9938	0.9943	10	0.202
Pauli-Z	0.9943	0.9943	10	0.183

vibrational transition of $v=1\leftrightarrow 0$ (2143 cm^{-1}) at any time, which keeps the population in the $v=0$ state in path (a) almost constant. On the other hand, the laser pulse contains relatively large intensities at the frequency resonant with the $v=2\leftrightarrow 1$ transition (2117 cm^{-1}) between $t=-1$ and 1 ps. The strong intensity at 2117 cm^{-1} induces the transition between the $v=1$ initial state and the $v=2$ auxiliary state in path (b) to achieve the phase rotation by π. In molecular vibrational states, anharmonicity makes the transition frequencies of $v=0\leftrightarrow 1$ and $v=2\leftrightarrow 1$ slightly different, which results in efficient Z gate operation.

The fidelity F and population transfer probability $\bar{P}$ for quantum gates using pure vibrational eigenstates for the $X(^1\Sigma^+)$ state of CO are summarized in Table I, together with the peak pulse intensities. Fairly good fidelities of over 98% are achieved for one-qubit quantum gates. An input laser pulse energy of about 10 μJ is enough to realize high fidelities.

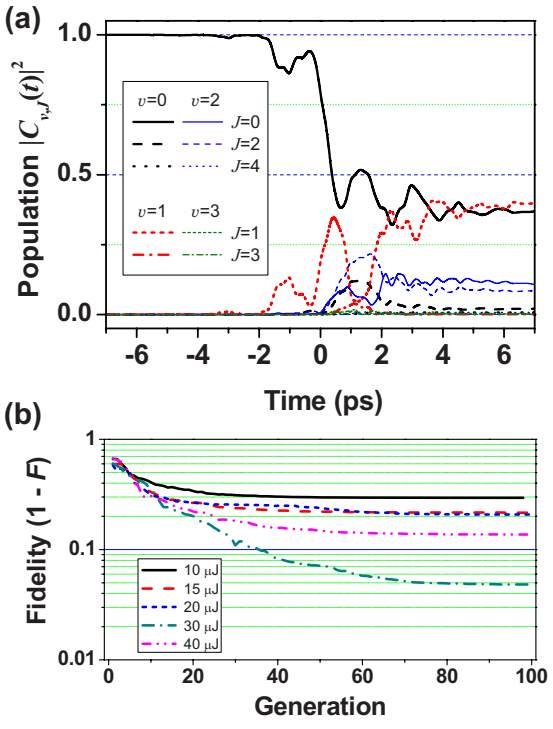

FIG. 5. (Color online) (a) Population transfers of path (a) in the Hadamard gate using rovibrational eigenstates with the input pulse energy of 15 μJ. (b) Input energy dependence on the convergence characterized by $1-F$, where F is the fidelity defined in Eq. (5), as a function of generation in the GA calculation.

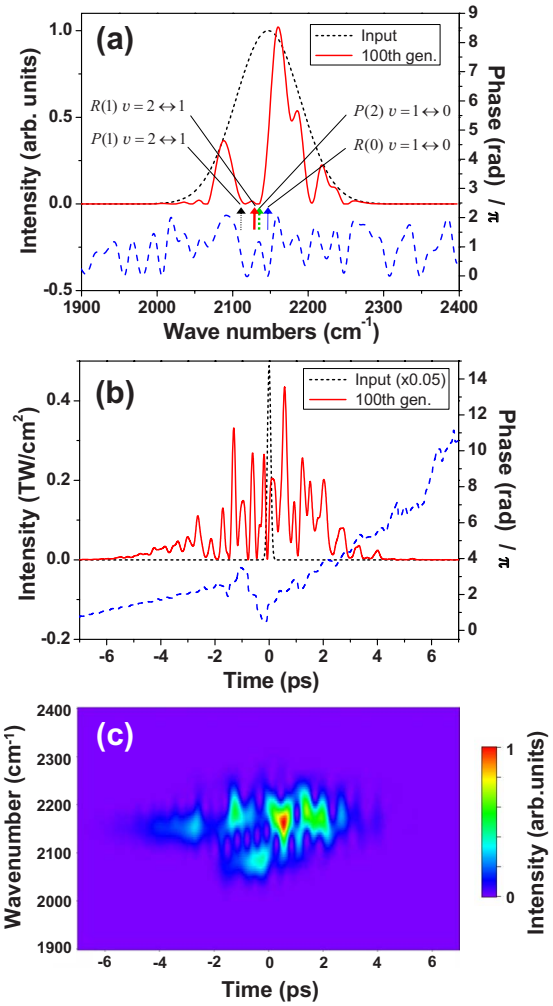

FIG. 6. (Color online) Optimized laser pulse for the Hadamard gate using the rovibrational eigenstates as qubits. The input pulse energy to the shaper was 30 μJ. The pulse shape is shown in (a) the frequency and (b) the time domain, and (c) as the Gabor transform calculated by Eq. (16). Dotted (black) and solid (red) lines in (a) and (b) show the shape of the input pulse and the optimized pulse after 100 generations of the GA, respectively. Dashed (blue) line shows the optimized phase function of the shaped pulse. The arrows indicate the transition frequencies involved in this gate operation. See Fig. 1 for the definition of the colors and styles.

B. Optimized electric fields for rovibrational quantum gates

In this section, we present the results for optimized laser pulse shapes that realize quantum gates using rotational-vibrational eigenstates. The number of transition pathways increases when the rotational degrees of freedom are taken into account, which makes the shaped laser pulse more complicated.

In order to solve the Schrödinger equation in Eq. (12), we expanded the time-dependent wave function $|\Psi(t)\rangle$ in terms of the $|JM\rangle$ rotational and $|v\rangle$ vibrational states as follows:

$$|\Psi(t)\rangle = \sum_v \sum_{JM} C_{v,JM}(t)|v\rangle|JM\rangle, \tag{20}$$

where $C_{v,JM}(t)$ is the complex amplitude of the state $|v\rangle|JM\rangle$. The rotational-vibrational states $|v\rangle|JM\rangle$ are the eigenstates

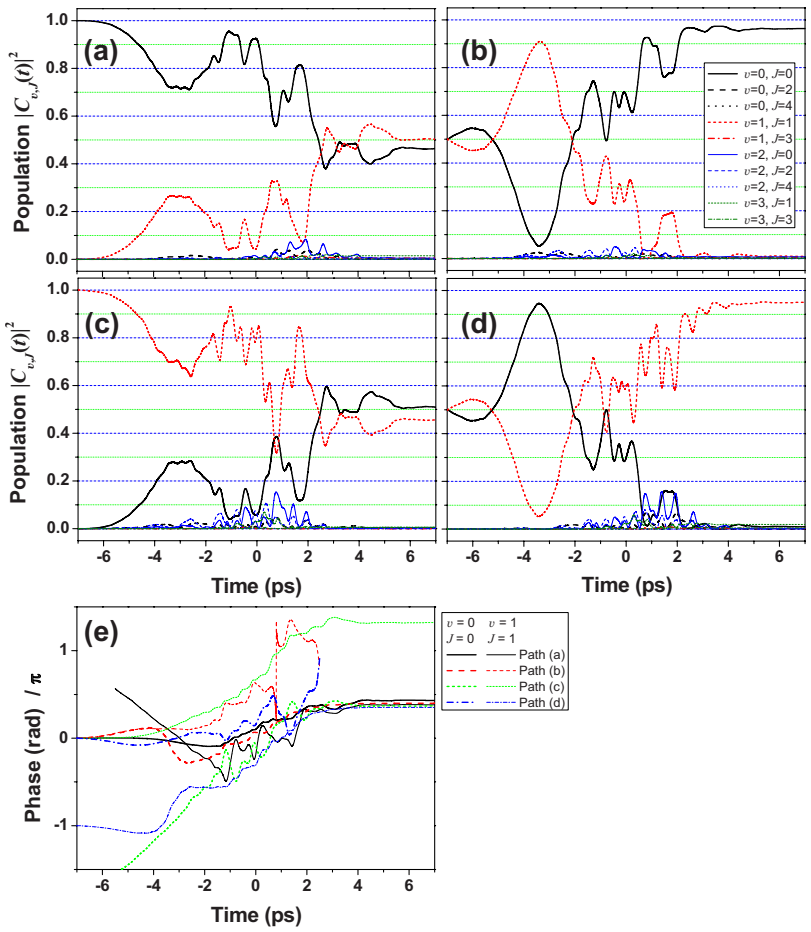

FIG. 7. (Color online) Population transfers and phase changes for the Hadamard gate induced by the laser pulse shown in Fig. 6 using the rovibrational eigenstates in the $X(^1\Sigma^+)$ state of CO. The input pulse energy was assumed to be 30 μJ in the calculation. (a)–(d) display the population transitions of paths (a)–(d) in the Hadamard gate, respectively. (e) shows the phase evolution of the vibrational eigenstates composing the wave packet in each path. Note that the phase is shown only when the population of the state is greater than 5%.

of the zero-order Hamiltonian H_0 in Eq. (12). In the present calculations, we have included from $v=0$ to 6 and $J=0$ to 8. The dipole interaction is described as

$$H_1(t) = -\vec{\mu}\cdot\vec{\varepsilon}(t) = -\mu\varepsilon(t)\cos\theta = -\mu\varepsilon(t)P_1(\cos\theta), \tag{21}$$

where $P_l(\cos\theta)$ is the Legendre polynomial of order l, and θ is the polar angle between the molecular axis and the polarization of the electric field of the linearly polarized light. The interaction via the polarizability is given by

$$H_2(t) = -\frac{1}{2}\vec{\varepsilon}(t)\cdot\vec{\alpha}\cdot\vec{\varepsilon}(t) = -\frac{1}{2}\varepsilon(t)^2\left(\alpha + \frac{2\gamma}{3}P_2(\cos\theta)\right), \tag{22}$$

where α and γ are the isotropic and anisotropic polarizabilities, respectively. Detailed expressions for the differential equation including these interaction terms used to obtain the rovibrational wave packet are discussed in our previous paper [27].

The selection rule of $\Delta J = \pm 1$ and $\Delta M = 0$ is derived for processes induced by the dipole moment, while the selection rule of $\Delta J = \pm 2, 0$ and $\Delta M = 0$ is derived for the interaction via the polarizabilities [27]. Since there is no interaction that connects $\Delta M \neq 0$, we omit the subscript M in the following discussion by setting $M=0$ all the time.

1. Hadamard gate

First, we examined the Hadamard gate. We treated the rovibrational states $|v=0, J=0\rangle$ and $|v=1, J=1\rangle$ as the qubits $|0\rangle$ and $|1\rangle$, respectively. These states are coupled via the $R(0)$ rovibrational transition. The laser electric field was optimized so as to achieve the four paths (a)–(d), described in Sec. III A 1. Figure 5(a) shows the population transfer of path (a) in the Hadamard gate by the optimized electric field. The laser input energy to the shaper was assumed to be 15 μJ in this calculation. After the interaction with the shaped laser field, the populations in the $|v=2, J=0\rangle$ and $|v=2, J=2\rangle$ rovibrational states still remain over 10%; this could not be reduced by a laser field whose input energy to the shaper was 15 μJ. As a result, the populations in the $|v=0, J=0\rangle$ and $|v=1, J=1\rangle$ states were both about 40% after the Hadamard gate operation. The fidelity of the operation shown in Fig. 5(a) was only $F=0.7835$.

The fidelity could be improved by increasing the input pulse energy to the shaper. Figure 5(b) shows the input energy dependence on the convergence speed of the GA and the quantum gate fidelity F for the Hadamard gate operation with rovibrational eigenstates. The vertical axis shows $1-F$. When the input pulse energy was as low as 10 μJ, the laser pulse field converged within 40 generations, but the fidelity for the Hadamard gate did not improve to better than $F=0.7$. As the input energy was increased to 30 μJ, the fidelity improved to $F=0.9518$. However, the higher input energy

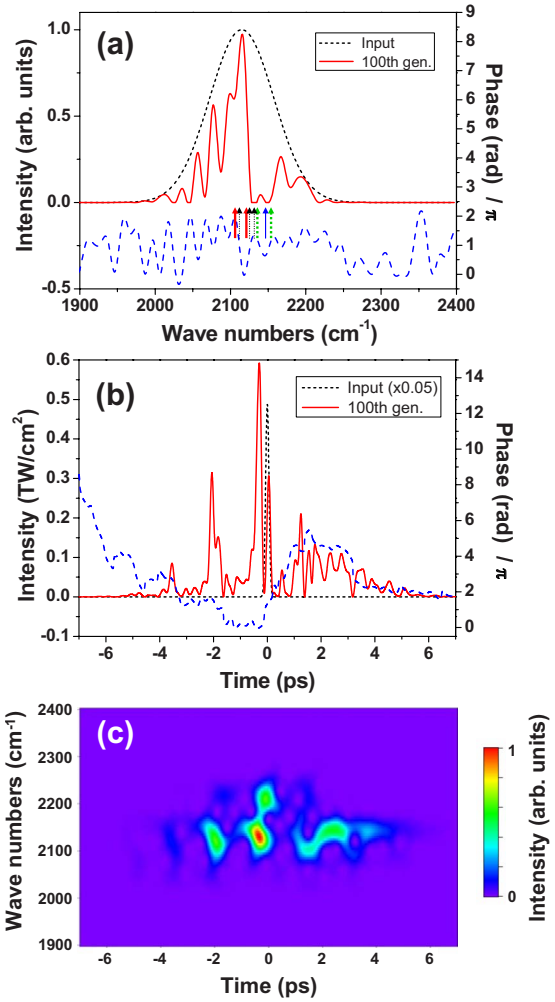

FIG. 8. (Color online) Optimized laser pulse for the CNOT gate defined as $|00\rangle \rightarrow |00\rangle$, $|01\rangle \rightarrow |01\rangle$, $|10\rangle \rightarrow |11\rangle$, and $|11\rangle \rightarrow |10\rangle$. The pulse shape is shown in (a) the frequency and (b) the time domain, and (c) as the Gabor transform calculated by Eq. (16). Dotted (black) and solid (red) lines in (a) and (b) show the shapes of the input pulse and the optimized pulse after 100 generations of the GA, respectively. Dashed (blue) line in (a) and (b) shows the optimized phase function of the shaped pulse. The arrows indicate the transition frequencies involved in this gate operation. See Fig. 1 for the definition of the colors and styles.

of 40 μJ gave worse fidelity than that at 30 μJ. Our GA method could not find the best laser field when the input energy was too strong. Figure 5(b) indicates that there is an optimal input energy for the quantum gate operation, and the input pulse energy is also an important input parameter for the optimization method.

We found that the fidelity for the Hadamard gate became maximum with the input pulse energy of 30 μJ when we treated the $|v=0,J=0\rangle$ and $|v=1,J=1\rangle$ rovibrational states as the qubits. This pulse energy is much larger than that of 7.5 μJ which gives the fidelity of $F=0.9834$ for the Hadamard gate with the pure vibrational state described in Sec. III A 1. Part of the reason for the high energy requirement for rovibrational qubits is the J dependence on the rovibrational transition probability. The transition probabilities for the $R(J)$ and $P(J)$ branches are obtained as $|\langle v',J+1|\vec{\mu}\cdot\vec{\varepsilon}|v'',J\rangle|^2 = P(J+1\leftrightarrow J) \propto (J+1)^2/(2J+1)(2J+3)$ and $|\langle v',J-1|\vec{\mu}\cdot\vec{\varepsilon}|v'',J\rangle|^2 = P(J-1\leftrightarrow J) \propto J^2/(2J+1)(2J-1)$, respectively, for the $M=0$ state. Since $P(1\leftrightarrow 0) \propto 1/3 \sim 0.333$ and $P(1\leftrightarrow 2) \propto 4/15 \sim 0.267$, three to four times larger pulse intensity is required for rovibrational quantum gate operations as compared to the gate operations with pure vibrational states.

Figure 6 shows the optimized electric field, and Fig. 7 shows the detailed behavior of the population transfers and phase changes for the Hadamard gate with input energy of 30 μJ. The temporal pulse width was stretched to about 8 ps, which is much longer than that for the case of pure vibrational qubits shown in Fig. 2. The fidelity of the operation was $F=0.9518$. During the interaction time, there are a couple of population exchanges (oscillation in population) between the $|v=0,J=0\rangle$ and $|v=1,J=1\rangle$ rovibrational states, while there is no significant population transfer to higher rovibrational states as seen in Fig. 7. As given in Fig. 7(e), the relative phases were well locked by the optimized laser field, with the phase evolution of the total system given by $\varphi \sim 3\pi/8$. The deviation of the phases between the $|v=0,J=0\rangle$ and $|v=1,J=1\rangle$ rovibrational states after the wave packet evolution was 0.025π, which is slightly larger than that of 0.011π for the pure vibrational qubits shown in Fig. 3(e).

The behavior of population transfers shown in Fig. 7 is quite similar to that shown in Fig. 3 for the pure vibrational qubits, while the electric field shown in Fig. 6 is completely different from that in Fig. 2. The electric field shown in Fig. 6 is longer and more complicated in the time domain than that shown in Fig. 2. In the frequency domain, the peak frequencies are different between Figs. 2 and 6. In the case of the pure vibrational qubits of $|0\rangle=|v=0\rangle$ and $|1\rangle=|v=1\rangle$, the transition frequency of $v=1\leftrightarrow 0$ is 2143 cm^{-1}, while that of $v=2\leftrightarrow 1$ is 2117 cm^{-1}. The frequency difference due to the anharmonicity is 26 cm^{-1}, which is larger than the resolution of the pulse shaper of 10 cm^{-1}. The electric field shown in Fig. 2 contains frequency at 2143 cm^{-1} with almost the maximum intensity, while the amplitude at 2117 cm^{-1} is almost null. The electric field shown in Fig. 2 is such that the pulse does not excite the unwanted $v=2\leftrightarrow 1$ transition. In the case of the rovibrational qubits of $|0\rangle=|v=0,J=0\rangle$ and $|1\rangle=|v=1,J=1\rangle$, the transition frequency between the two levels is 2147 cm^{-1}. Other transitions which are accessible from these two levels are $P(2)$ $v=1\leftrightarrow 0$, $R(1)$ $v=2\leftrightarrow 1$, and $P(1)$ $v=2\leftrightarrow 1$ whose transition frequencies are 2136, 2124, and 2113 cm^{-1}, respectively, as shown in Fig. 1. As seen in Fig. 6(a), the amplitudes at the latter three frequencies are almost null. On the other hand, the amplitude at 2147 cm^{-1} is not maximum. Since the frequency difference between the transitions $R(0)$ $v=1\leftrightarrow 0$ and $P(2)$ $v=1\leftrightarrow 0$ is only 11 cm^{-1}, which is comparable to the resolution of the shaper, the amplitude at the transition $R(0)$ $v=1\leftrightarrow 0$ cannot be the maximum. In general, since the energy separations of rovibrational transitions are much closer than those of vibrational transitions without rotational excitation, quantum gate operations using rovibrational states are more difficult than those using pure vibrational states manipulated by broadband laser pulses. This must be the reason

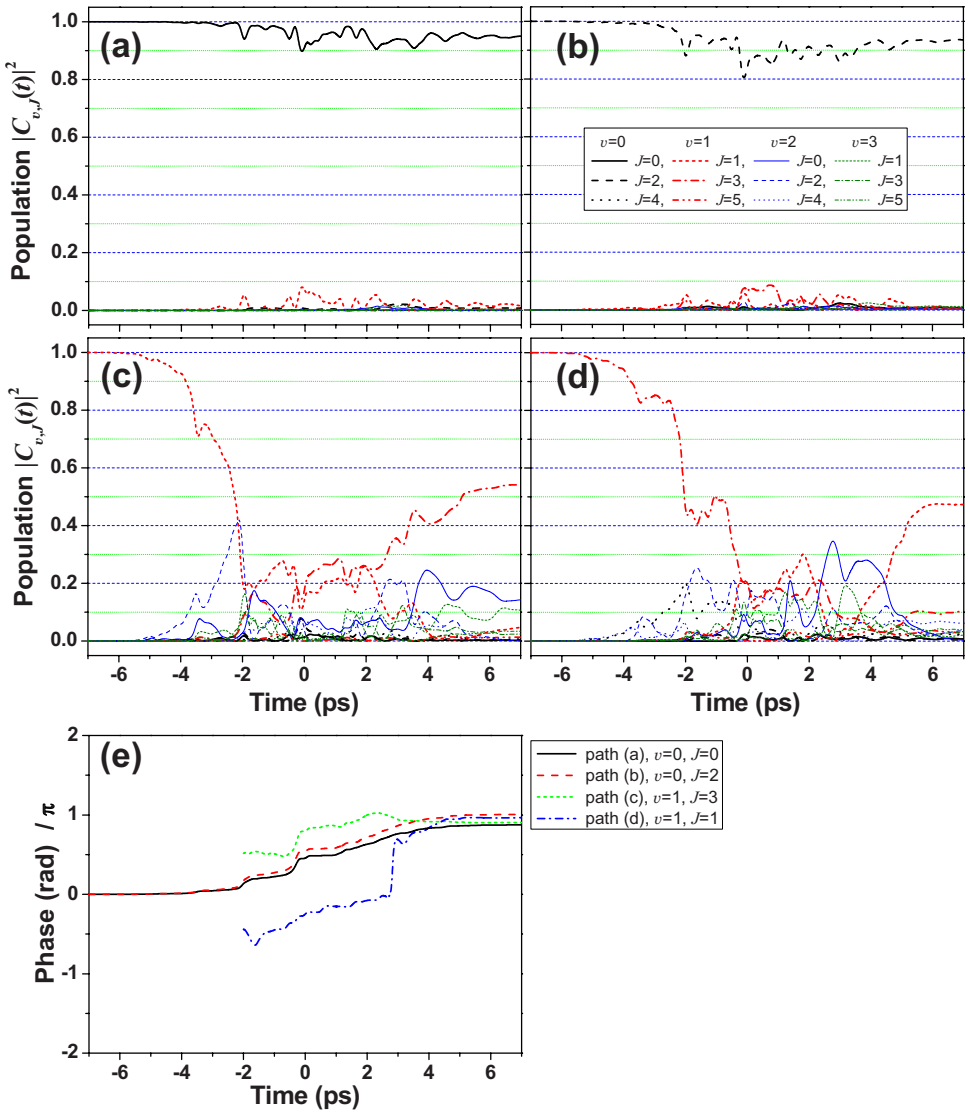

FIG. 9. (Color online) Population transfers and phase changes for the CNOT gate induced by the laser pulse shown in Fig. 8 using the rovibrational eigenstates. The input pulse energy was assumed to be 30 μJ in the calculation. (a)–(d) display the population transitions of paths (a)–(d) in the CNOT gate, respectively. (e) shows the phase evolution of the vibrational eigenstates. Note that the phase is shown only when the population of the state is greater than 5%.

for the fidelity for rovibrational qubits shown in Figs. 6 and 7 being worse than that for the pure vibrational qubits shown in Figs. 2 and 3.

We have also optimized the electric field to realize the NOT gate with rovibrational eigenstates as another example of one-qubit gate operations. The optimized laser field (not shown) realized the NOT gate with a fidelity of $F=0.9646$ when the laser input energy to the shaper was assumed to be 30 μJ. This fidelity is better than that for the Hadamard gate, but worse than that for the NOT gate with the pure vibrational states. The laser pulse was considerably stretched to ~8 ps as in the case of the Hadamard gate.

2. CNOT gate

In this section, we examine the CNOT gate, which is a fundamental two-qubit operation, with rovibrational qubits defined as $|00\rangle=|v=0,J=0\rangle$, $|01\rangle=|v=0,J=2\rangle$, $|10\rangle=|v=1,J=1\rangle$, and $|11\rangle=|v=1,J=3\rangle$. The optimized laser field was calculated so as to achieve the following four transitions: path (a), $|00\rangle\rightarrow|00\rangle$, path (b), $|01\rangle\rightarrow|01\rangle$, path (c), $|10\rangle\rightarrow|11\rangle$, and path (d): $|11\rangle\rightarrow|10\rangle$, simultaneously, by considering the vibrational and rotational states as the control and target qubits, respectively. The latter two paths are induced by two-photon transitions of $P(2)$ $v=1\leftrightarrow0$ and $R(2)$ $v=1\leftrightarrow0$, or $R(1)$ $v=2\leftrightarrow1$ and $P(3)$ $v=2\leftrightarrow1$. Note that this two-photon transition is induced by sequential dipole transitions [Eq. (21)] and is not due to interaction via polarizability [Eq. (22)]. This is because the dipole interaction is much larger than interaction via polarizability when the pulse includes the resonant frequencies.

Figure 8 shows the optimized laser field. The center frequency of the input pulse used in the calculation was 2115 cm^{-1}, slightly shifted to lower frequency as compared to that for other calculations. We found that shift improved the fidelity for the CNOT gate. Figure 9 shows the optimized behavior of the population transfers and phase rotations for each path. The initial input energy of 30 μJ was assumed. As seen in Figs. 9(c) and 9(d), the populations in the $|v=1,J=3\rangle$ state in path (c) and in the $|v=1,J=1\rangle$ state in path (d) are only 50% or so after the wave packet propagation. Although the dispersion of the phase during the gate operation was relatively small (0.132π), the population transfers in paths (c) and (d) were not sufficient. As a result, the fidelity was obtained as only $F=0.6877$, while the efficiency of the population transfers defined in Eq. (19) was

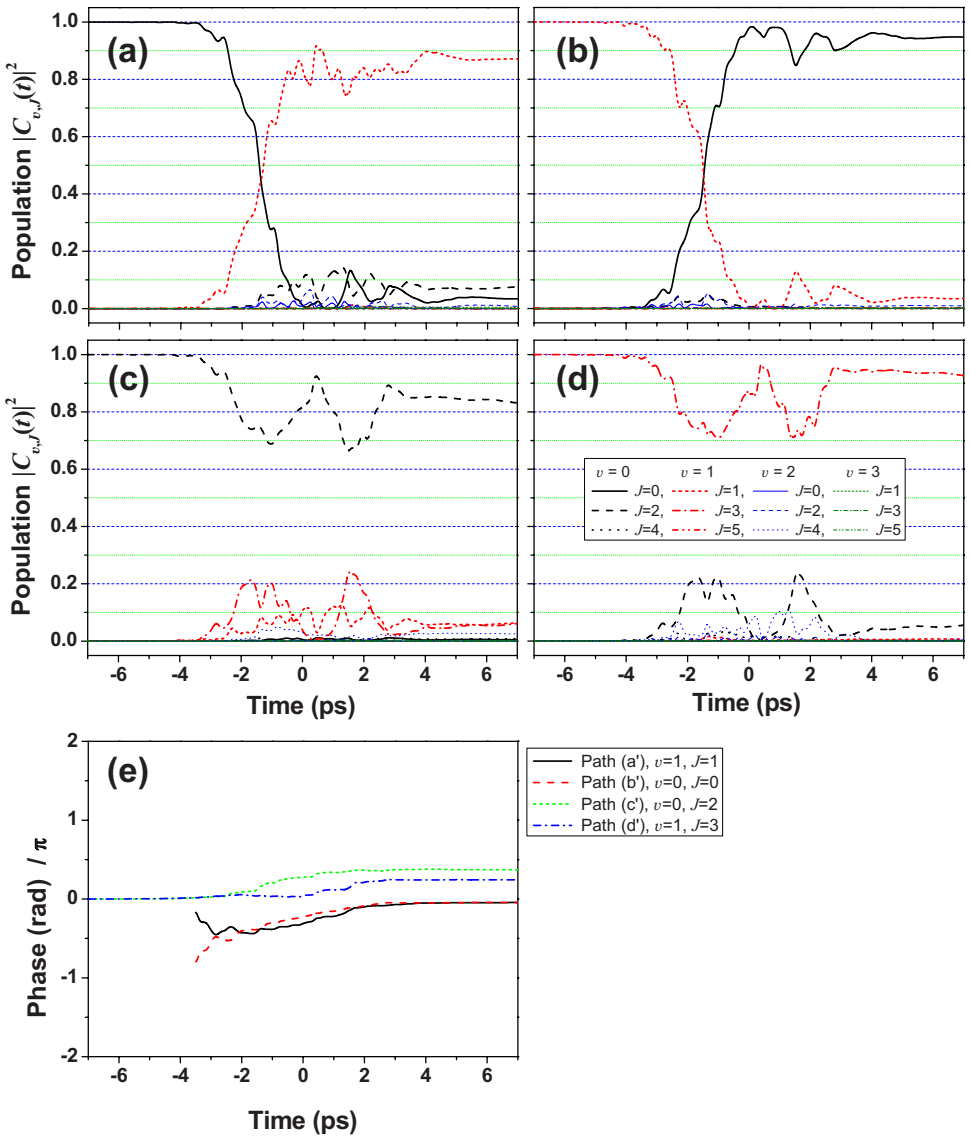

FIG. 10. (Color online) Population transfers by the optimized laser pulse for the ACNOT gate using rovibrational eigenstates defined as (a) $|00\rangle \rightarrow |10\rangle$, (b) $|10\rangle \rightarrow |00\rangle$, (c) $|01\rangle \rightarrow |01\rangle$, and (d) $|11\rangle \rightarrow |11\rangle$. The input pulse energy was assumed to be 20 μJ in the calculation. (e) shows the phase evolution of the vibrational eigenstates. Note that the phase is shown only when the population of the state is greater than 5%.

$\bar{P}=0.7249$. These numbers indicate that good efficiency of population transfer is difficult to achieve in the CNOT gate operation when the rotational states are treated as the target bit.

As another example, we have examined the gate operation that includes the four transitions path (a′), $|00\rangle \rightarrow |10\rangle$, path (b′), $|10\rangle \rightarrow |00\rangle$, path (c′), $|01\rangle \rightarrow |01\rangle$, and path (d′), $|11\rangle \rightarrow |11\rangle$, simultaneously. This gate operation corresponds to an alternative CNOT (ACNOT) gate when the second qubit is considered as the control qubit. In this case, the vibrational states are treated as the target and the rotational states as the control qubits, as opposed to the previous example. In this case, paths (a′) and (b′) are achieved by the one-photon transition $R(0)$ $v=1 \leftrightarrow 0$. The obtained electric field (not shown) results in the population transfers and phase rotations shown in Fig. 10. The center frequency of the input pulse was set to be 2147 cm^{-1}. Even with the weaker input pulse of 20 μJ, the population transfers in paths (a′) and (b′) are better than 85%, and the obtained population transfer probability was $\bar{P}=0.8942$. The reason for the better population transfer probability in the second example (v, target, J, control) than the first example (v, control, J, target) is that paths (a′) and (b′) in the second example are one-photon allowed, while paths (c) and (d) in the first example are one-photon forbidden.

Despite the fact that the population transfer probability of the second example was much better than in the first example, the fidelity of the second example was obtained to be $F=0.6374$, which is about the same as in the first CNOT example. The phase control is more difficult in the two-qubit operation than in the one-qubit operations. Part of the reason for the difficulty in control is the proximity between desired and undesired transitions as indicated by arrows in Fig. 8(a).

The fidelity F and population transfer probability $\bar{P}$ for the quantum gates using rovibrational eigenstates for the $X(^1\Sigma^+)$ state of CO are summarized in Table II, together with the peak intensity for the shaped pulse. The fidelities for the one-qubit system shown in Table II are slightly worse than those shown in Table I, but they are not significantly worse. The input laser pulse energies required for one-qubit quantum gate operations with rovibrational transitions are higher than those with pure vibrational transitions, but a power of 30 μJ will be experimentally available soon in the mid-ir

TABLE II. The efficiency of quantum gate operations with rovibrational eigenstates in the $X(^1\Sigma^+)$ state of CO. CNOT (a) and ACNOT (b) correspond to the results shown in Figs. 9 and 10, respectively.

Gate	F	$\bar{P}$	Input energy (μJ)	Peak intensity (TW/cm^2)
Hadamard	0.9518	0.9585	30	0.434
NOT	0.9646	0.9648	30	0.297
CNOT (a)	0.6877	0.7249	30	0.592
ACNOT (b)	0.6374	0.8942	20	0.232

region by use of high-power ultrafast laser amplifier systems. Therefore, one-qubit quantum gate operations on rovibrational states of molecules are proved to be experimentally feasible by the present calculation, although more improvement is required to satisfy the threshold condition for fault-tolerant calculation [52].

For two-qubit operations with rotation (J) and vibration (v) on a single CO molecule, the fidelities shown in Table II are not acceptable for practical computation. In order to achieve better fidelity for the CNOT gate operation using rovibrational states as qubits, we may need better resolution than 10 cm^{-1} for the shaper. This is because the frequency separations among transitions involved in the gate operation are smaller than 10 cm^{-1}, e.g., the frequency separation between $v=1, J=1 \leftrightarrow v=0, J=0$ and $v=1, J=3 \leftrightarrow v=0, J=2$ is only 8 cm^{-1}, so that it is difficult to excite them individually. In other words, the rovibrational states in the $X(^1\Sigma^+)$ state of CO are not the best system as the qubit because of its small rotational constant $B \sim 1.9$ cm^{-1}. In order to control the population and phase of rovibrational wave packets more precisely by shaped mid-ir pulses, systems with larger rotational constants are preferable. The $X(^2\Pi_{3/2})$ state of OH ($B \sim 19$ cm^{-1}) may be such a candidate. Calculations for this system will prove whether we can use the rotational (J) and vibrational (v) degrees of freedom as two independent qubits for two-qubit quantum gate operations. This effort is in progress.

IV. CONCLUSION

In this paper, we have numerically examined the experimentally feasible shape of ultrafast pulses needed to realize molecular qubit operations. We have optimized the shape of a laser pulse in the frequency domain, since conventional pulse shapers operate in the frequency domain. For this purpose, the GA is more appropriate than OCT, since OCT iteratively solves the differential equations in the time domain and it seems to be difficult to impose the experimental limitations required in the frequency domain.

The present results demonstrate both the potential and difficulties in the application of rovibrational states to quantum computation. It is shown that one-qubit operations can be achieved with high fidelity. As demonstrated in the CNOT gate operation, however, the fidelity of the two-qubit system is still far too low for quantum computation. In order to improve the fidelity of two-qubit gate operations, we may need to use a pulse shaper with high frequency resolution (<10 cm^{-1}), or find a better molecular system whose rovibrational transition frequencies are well separated compared with the resolution of the shaper.

In order to perform an actual calculation such as the Deutsch-Jozsa algorithm, one must apply the present method to multiple vibrational states of polyatomic molecules or spatially aligned molecules. The next effort of our study will be the investigation of multiqubit systems using eigenstates of polyatomic molecules or an ensemble of trapped molecules; this is currently under way.

ACKNOWLEDGMENTS

This research was supported by the Japan Science and Technology Agency under the CREST project "Quantum Information Processing" and by NSERC. This research has been enabled by the use of WestGrid computing resources, which are funded in part by the Canada Foundation for Innovation, Alberta Innovation and Science, BC Advanced Education, and the participating research institutions. WestGrid equipment is provided by IBM, Hewlett Packard, and SGI.

[1] M. Dantus and V. V. Lozovoy, Chem. Rev. **104**, 1813 (2004), and references therein.
[2] U. Gaubatz, P. Rudecki, S. Schiemann, and K. Bergmann, J. Chem. Phys. **92**, 5363 (1990).
[3] N. V. Vitanov, K. A. Suominen, and B. W. Shore, J. Phys. B **32**, 4535 (1999).
[4] N. V. Vitanov, T. Halfmann, B. W. Shore, and K. Bergmann, Annu. Rev. Phys. Chem. **52**, 763 (2001).
[5] D. Sugny, C. Kontz, M. Ndong, Y. Justum, G. Dive, and M. Desouter-Lecomte, Phys. Rev. A **74**, 043419 (2006).
[6] C. Menzel-Jones and M. Shapiro, Phys. Rev. A **75**, 052308 (2007).
[7] J. P. Palao and R. Kosloff, Phys. Rev. Lett. **89**, 188301 (2002).
[8] J. P. Palao and R. Kosloff, Phys. Rev. A **68**, 062308 (2003).
[9] D. Deutsch and R. Jozsa, Proc. R. Soc. London, Ser. A **439**, 553 (1992).
[10] J. Vala, Z. Amitay, B. Zhang, S. R. Leone, and R. Kosloff, Phys. Rev. A **66**, 062316 (2002).
[11] Y. Ohtsuki, Chem. Phys. Lett. **404**, 126 (2005).
[12] F. Eickemeyer, R. A. Kaindl, M. Woerner, T. Elsaesser, and A. M. Weiner, Opt. Lett. **25**, 1472 (2000).
[13] T. Witte, D. Zeidler, D. Proch, K. L. Kompa, and M. Motzkus, Opt. Lett. **27**, 131 (2002).
[14] H. S. Tan and W. S. Warren, Opt. Express **11**, 1021 (2003).
[15] N. A. Naz, H. S. S. Hung, M. V. O'Connor, D. C. Hanna, and D. P. Shepherd, Opt. Express **13**, 8400 (2005).
[16] S. H. Shim, D. B. Strasfeld, E. C. Fulmer, and M. T. Zanni, Opt. Lett. **31**, 838 (2006).

[17] M. Tsubouchi and T. Momose, J. Opt. Soc. Am. B **24**, 1886 (2007).
[18] D. B. Strasfeld, S. H. Shim, and M. T. Zanni, Phys. Rev. Lett. **99**, 038102 (2007).
[19] C. Gollub, U. Troppmann, and R. de Vivie-Riedle, New J. Phys. **8**, 48 (2006).
[20] C. M. Tesch, L. Kurtz, and R. de Vivie-Riedle, Chem. Phys. Lett. **343**, 633 (2001).
[21] C. M. Tesch and R. de Vivie-Riedle, Phys. Rev. Lett. **89**, 157901 (2002).
[22] U. Troppmann, C. M. Tesch, and R. de Vivie-Riedle, Chem. Phys. Lett. **378**, 273 (2003).
[23] C. M. Tesch and R. de Vivie-Riedle, J. Chem. Phys. **121**, 12158 (2004).
[24] U. Troppmann and R. de Vivie-Riedle, J. Chem. Phys. **122**, 154105 (2005).
[25] B. M. R. Korff, U. Troppmann, K. L. Kompa, and R. de Vivie-Riedle, J. Chem. Phys. **123**, 244509 (2005).
[26] D. Babikov, J. Chem. Phys. **121**, 7577 (2004).
[27] M. Tsubouchi, A. Khramov, and T. Momose, Phys. Rev. A **77**, 023405 (2008).
[28] S. Suzuki, K. Mishima, and K. Yamashita, Chem. Phys. Lett. **410**, 358 (2005).
[29] K. Shioya, K. Mishima, and K. Yamashita, Mol. Phys. **105**, 1283 (2007).
[30] M. M. Wefers and K. A. Nelson, J. Opt. Soc. Am. B **12**, 1343 (1995).
[31] M. A. Dugan, J. X. Tull, and W. S. Warren, J. Opt. Soc. Am. B **14**, 2348 (1997).
[32] D. E. Goldberg, *Genetic Algorithms in Search, Optimization and Machine Learning* (Addison-Wesley, Reading, MA, 1997).
[33] V. F. Krotov, Autom. Remote Control (Engl. Transl.) **34**, 1863 (1973).
[34] V. G. Krotov, Autom. Remote Control (Engl. Transl.) **35**, 1 (1974).
[35] V. F. Krotov, Autom. Remote Control (Engl. Transl.) **35**, 345 (1974).
[36] J. Somlói, V. A. Kazakov, and D. J. Tannor, Chem. Phys. **172**, 85 (1993).
[37] W. S. Zhu, J. Botina, and H. Rabitz, J. Chem. Phys. **108**, 1953 (1998).
[38] W. S. Zhu and H. Rabitz, J. Chem. Phys. **109**, 385 (1998).
[39] Y. Ohtsuki, G. Turinici, and H. Rabitz, J. Chem. Phys. **120**, 5509 (2004).
[40] P. Gross, D. Neuhauser, and H. Rabitz, J. Chem. Phys. **96**, 2834 (1992).
[41] T. Hornung, M. Motzkus, and R. de Vivie-Riedle, J. Chem. Phys. **115**, 3105 (2001).
[42] R. S. Judson and H. Rabitz, Phys. Rev. Lett. **68**, 1500 (1992).
[43] D. Zeidler, S. Frey, K. L. Kompa, and M. Motzkus, Phys. Rev. A **64**, 023420 (2001).
[44] W. H. Press, B. P. Flannery, S. A. Teukolsky, and W. T. Vetterling, *Numerical Recipes in C* (Cambridge University Press, Cambridge, U.K., 1988).
[45] A. W. Mantz, J. P. Maillard, W. B. Roh, and K. N. Rao, J. Mol. Spectrosc. **57**, 155 (1975).
[46] D. Goorvitch and C. Chackerian, Astrophys. J., Suppl. Ser. **91**, 483 (1994).
[47] J. O. Hirschfelder, C. F. Curtis, and R. B. Bird, *Molecular Theory of Gases and Liquids* (Wiley, New York, 1954).
[48] T. Witte, T. Hornung, L. Windhorn, D. Proch, R. de Vivie-Riedle, M. Motzkus, and K. L. Kompa, J. Chem. Phys. **118**, 2021 (2003).
[49] L. Windhorn, J. S. Yeston, T. Witte, W. Fuss, M. Motzkus, D. Proch, K. L. Kompa, and C. B. Moore, J. Chem. Phys. **119**, 641 (2003).
[50] T. Witte, J. S. Yeston, M. Motzkus, E. J. Heilweil, and K. L. Kompa, Chem. Phys. Lett. **392**, 156 (2004).
[51] M. Sugawara and Y. Fujimura, J. Chem. Phys. **100**, 5646 (1994).
[52] M. A. Nielsen and I. L. Chuang, *Quantum Computation and Quantum Information* (Cambridge University Press, Cambridge, U.K., 2001).